The Effect of a Micro-Perforated Cavity Floor on the Propagation of Tunnel-Cavity Modes in a Low-Speed Duct Flow

Cédric Maury, Teresa Bravo, Daniel Mazzoni

THE EFFECT OF A MICRO-PERFORATED CAVITY FLOOR ON THE PROPAGATION OF TUNNEL-CAVITY MODES IN A LOW-SPEED DUCT FLOW

Cédric Maury[1] **Teresa Bravo[2]** **Daniel Mazzoni[3]**

[1] Aix-Marseille Univ., CNRS, Centrale Marseille, Laboratoire de Mécanique et d'Acoustique (LMA), 4, impasse Nikola Tesla, 13013 Marseille, France
[2] Consejo Superior de Investigaciones Cientificas (CSIC), ITEFI-CSIC, Serrano 144, 28006, Madrid, Spain
[3] Aix-Marseille Univ., CNRS, Centrale Marseille, Institut de Recherche sur les Phénomènes Hors-Equilibres (IRPHE), 49, rue Frédéric Joliot-Curie, 13013 Marseille, France
cedric.maury@centrale-marseille.fr

ABSTRACT

Experimental and numerical studies are presented that show how transverse Tunnel-Cavity (TC) modes are nearly trapped and attenuated by a non-symmetric shallow cavity whose base wall is micro-perforated and that undergoes a low-speed flow regime at Mach 0.09. Three effects are pointed out. First, wall-pressure measurements and 2D LBM (Lattice-Boltzmann Method) simulations confirmed the potential of micro-perforated cavity floors to attenuate the transverse cut-on TC modes that are cut-off in the tunnel section and excited by the shear layer, albeit overestimated in the 2D simulations. LBM simulations show that the maximum velocity fluctuations occur within, but also at the inlet/outlet of the micro-perforations through vortex shedding. The latter mechanism appears to play a more important role in the attenuation than visco-thermal dissipation, given a Shear number comprised between 2.9 and 5.1 up to 1 kHz. Second, elasto-acoustic coupling was observed between the transverse TC resonances and the flexural modes of the thin micro-perforated panel, that causes a downshift of the first TC-Panel resonance frequencies with respect to the uncoupled TC resonances. Third, an optimisation study has been carried out on the micro-perforated panel (MPP) parameters for the MPP input impedance to achieve maximum axial decay rate of the least attenuated TC mode at its resonance frequency. Although this mode was already attenuated by the nominal MPP, simulations showed that replacing the cavity floor by an optimized MPP provides further broadband reduction in the region of the plane wave least attenuated mode below the first TC cut-on frequency. However, this effect is limited to the spatial extent where the axial mean flow velocity takes the value assumed in the optimisation process.

1. INTRODUCTION

The pressure fluctuations generated by a flow passing over an unbacked shallow cavity is a subject of importance for the transportation industry, but also in building acoustics. Some applications concern the design of deployable low-noise high-drag perforated spoilers mounted on aircraft wings [1], perforated cladding panels wrapped around buildings that monitor the exposure to light but that are inclined to generate wind-induced noise disturbances over the facades [2] and micro-perforated panels (MPP) inserted within double-glazed ventilation window systems [3].

The objective of the present work is to examine the effect of a micro-perforated base wall on the mitigation of the flow-induced noise over shallow unbacked cavities, more precisely on the attenuation of the pressure fluctuations induced by a shear layer of flow over such a cavity in transitional regime. When this regime takes place, flow reattachment might occur at the cavity floor. It has been observed for cavities with a length-to-depth ratio comprised between 8 and 13 [4], but it has not been studied systematically. An extensive review has been provided by Gloerfelt [5] on the driving mechanisms and main parameters that govern the dynamics of flow past a cavity together with a state-of-the-art of the theoretical and numerical models that predict the observed tonal and broadband pressure components. He stressed the importance of the tunnel (T) modes that occur in wind-tunnel or flow duct experiments. When a cavity is flush-mounted in the test section, experimental [6] and simulation studies [7,8] showed that the noise frequency spectra is dominated by tonal peaks due to transverse acoustic modes that occur within the height of the duct above the cavity. Micro-perforating the cavity floor is a passive noise reduction strategy of potential interest, that does not provide additional weight nor further drag to the already high friction values induced by the shallow cavity over the flow.

Results from wind-tunnel measurements are presented in Sec. 2 for the effect of a MPP floor on the base wall-pressure fluctuations in a transitional flow cavity regime. Sec. 3 analyses the elasto-acoustic coupling between the MPP structural modes and the test section transverse acoustic modes. Sec. 4 presents results from a Lattice-

Boltzmann numerical scheme implemented to analyse the attenuation mechanisms at work induced by the MPP apertures on the resonance peaks. Sec. 5 presents an optimisation study that shows the effect of an optimized MPP floor on the pressure level fluctuations in a transitional flow cavity regime. Sec. 6 summarizes the main results and perspectives.

2. WIND-TUNNEL EXPERIMENTS

Experiments have been carried out in the test section of the IRPHE closed-loop wind-tunnel [9] to acquire the pressure fluctuations induced by a low-speed turbulent boundary layer (TBL) of air ($U_\infty = 30.7$ m s^{-1}) over the floor of a transitional shallow cavity with length 0.53 m, width 0.41 m and depth $D = 0.05$ m, so that the length-to-depth ratio of the cavity amounts to 10.6. As shown in Fig. 1, the cavity is flush-mounted over the top of the wind-tunnel test section with height $H = 0.9$ m. The MPP floor is a clamped aluminium panel of thickness 1 mm, micro-perforated with circular holes of diameter 0.5 mm with a perforation ratio of 0.8%, so that the holes pitch is 5 mm. The MPP no flow side radiates inside a wall-treated enclosure.

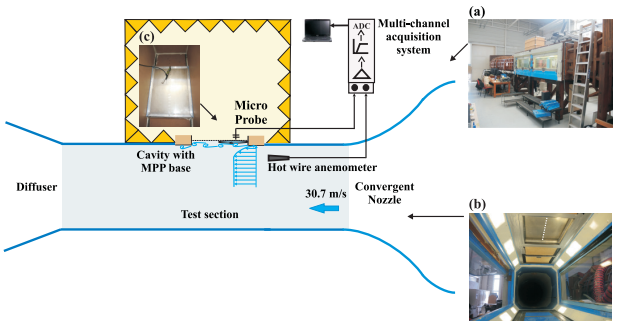

Figure 1. Overview of the experimental set-up used to measure wall-pressures on the base wall of plain or micro-perforated flow cavities: (a) the IRPHE low-speed wind-tunnel facility; (b) inner view of the test section on top of which is mounted a shallow transitional cavity: the white points represent the measurements positions over the cavity base wall; (c) view from the transmission room of the micro-probe pressure sensor used to measure the wall-pressure fluctuations on the cavity floor.

Wall-pressure measurements were performed using a pinhole micro-probe GRAS 40SC with diameter 1.25 mm and length 20 mm. It was sequentially flush-mounted at 19 positions over a streamwise line on the cavity floor. Each position was separated from each other by 28 mm. As the probe was displaced towards the upstream cavity edge, one observed a steady decay of the broadband wall-pressure fluctuations and a clear emergence of tonal peaks, at least within the first 18 cm of the cavity, as shown by the black curve of Fig. 2. These peaks occur in a non-symmetric cavity section under a subsonic flow. As observed in [10,11] and in Sec. 4 of this paper, they correspond to cut-on Tunnel-Cavity (TC) modes that are cut-off in the tunnel section. A detailed analysis in [10] shows that these are "nearly trapped" modes with small radiation leakage and high amplitude in the TC section.

As seen in Fig. 2, microperforating the base wall of the transitional cavity reduces by up to 8 dB the amplitudes of the dominant peaks between 300 Hz and 3 kHz. Figure 3 shows the spatial extent over which the wall-pressure spectra at the dominant peaks are attenuated by the MPP. One observes on all the subplots an attenuation zone that extends over one third of the cavity length towards the upstream edge, roughly corresponding to the size of the flow recirculation zone. It can be seen that, further downstream, the MPP is inefficient to attenuate the wall-pressure fluctuations. It even generates additional noise, in this zone at 1800 Hz [see Fig. 3(d)], due to back-scattering of the aerodynamic wall-pressures as the frequency increases [12]. Hence, a cost-efficient strategy for reducing the base wall-pressures would be to only micro-perforate part of the floor beneath the recirculation zone in order to achieve attenuation of the dominant peaks without enhancing the aerodynamic wall-pressures further downstream.

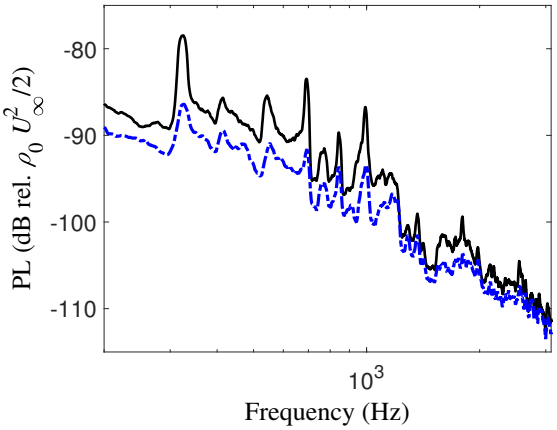

Figure 2. Base wall pressure level (PL) spectra measured at 9.8 cm from the upstream edge of a transitional cavity with plain (solid black) or microperforated (dash-dotted blue) floor.

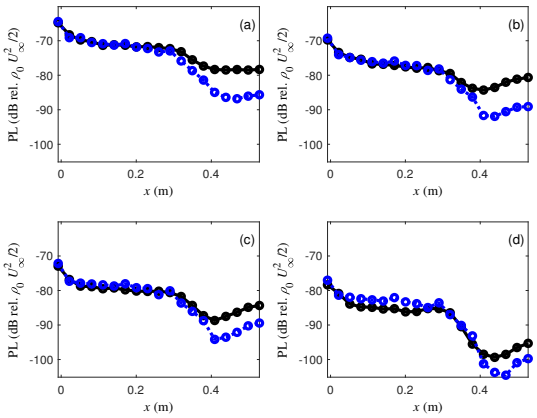

Figure 3. Spatial distribution of the pressure levels (PL) measured along 19 observation points over the base wall of a transitional cavity whose floor was either plain (solid black) or microperforated (dashed blue) at the frequencies (a) 324 Hz, (b) 690 Hz, (c) 990 Hz and (d) 1800 Hz.

3. ELASTO-ACOUSTIC COUPLING

The dominant peaks observed in Fig. 2 occur at 324 Hz, 536 Hz and 690 Hz. They occur systematically below the expected frequency range bounded by the TC and T transverse resonance frequencies, respectively given by $f_{n_z,TC} = n_z c_0/(H+D)$ and $f_{n_z,T} = n_z c_0/H$, with n_z the transverse modal order and c_0 the sound speed. For $2 \le n_z \le 4$, this corresponds to the following respective intervals: 358 – 378 Hz, 536 – 566 Hz and 715 – 755 Hz. Note that the first-order resonance should occur within the interval 179 – 189 Hz, but it was not detected because it was masked by the aerodynamic broadband noise, as it can be seen from Fig. 4(a) (blue curves). It however appears in the no-flow case when considering a pure acoustic excitation [Fig. 4(a), green curves]. Previous works on trapped TC resonances [10,11] assumed that the cavity-duct boundaries were rigid. This is not the case here since one observed flexural vibrations of the cavity floor induced by the 1 mm thick plain or micro-perforated panels. The panels flexural modes have been identified from laser vibrometer measurements [12] performed by transparency through a thick rigid block of Plexiglas flush-mounted at the bottom wall of the test section.

The effects of the panel elasticity on the first TC transverse resonances are now analysed. The acousto-elastic resonance frequencies of the Tunnel Cavity–Panel (TC–P) system can be expressed as a function of the TC and of the clamped panel uncoupled resonance frequencies, as follows [13, 14]

$$f^{\pm}_{np,TC-P} = \frac{1}{2\pi\sqrt{2}}\sqrt{\omega_n^2+\omega_p^2+C_{np} \pm D_{np}}, \qquad (1)$$

in which $D_{np} = \sqrt{\left(\omega_n^2-\omega_p^2\right)^2 + 2C_{np}\left(\omega_n^2+\omega_p^2\right)+C_{np}^2}$, $\omega_n = 2\pi f_{n,TC}$ and ω_p are the angular natural frequencies of the TC and of the clamped panel, respectively. The coefficient C_{np} describes the degree of spatial coupling between the p^{th} panel mode, G_p, and the trace on the panel surface S_P of the n^{th} TC mode, F_n. It reads $C_{np} = \rho_0 c_0^2 L_{np}^2/\left[\rho_P h_P (H+D_T) M_n M_p\right]$, with ρ_P the panel density, h_P the panel thickness, $L_{np} = A_P^{-1}\iint_{S_P} F_n G_p d^2S$, the modal coupling coefficient, and $M_p = A_P^{-1}\iint_{S_P} G_p^2 d^2S$ the modal mass with $M_n = 1/2$ for $n \ge 2$.

Fig. 4(b) shows the evolution of the natural acousto-elastic frequencies, $f^{\pm}_{1-(3,1),TC-P}$ and $f^{\pm}_{2-(5,1),TC-P}$, of the TC–P system of overall height $H+D = 0.95$ m when varying the aluminium panel thickness from 0.1 mm to 2 mm. The panel natural frequencies increase linearly with h_P unlike the TC acoustic resonance frequencies which only depend on the fluid domain property. For a 1 mm thin panel, one finds that the uncoupled first (resp. second) transverse TC resonances coincide with the (3,1) [resp. (5,1)] structural panel (P) resonances. Strong coupling between these TC and P modes, whose resonance frequencies coincide, leads to a significant veering of the acousto-elastic TC–P natural frequencies around $h_P = 1$ mm. Elasticity of the cavity floor is thus responsible for the downshift observed on the first TC resonances, $f_{1,TC}$ and $f_{2,TC}$: from 179 Hz down to 134 Hz due to coupling of the first TC resonance with the (3,1) panel mode and from 360 Hz down to 324 Hz due to coupling of the second TC resonance with the (5,1) panel mode. For thicker plates, elasticity effects can be neglected since the TC–P coupled resonances tend towards the uncoupled TC acoustic resonances. For plates thinner than 0.4 mm, the TC–P coupled resonances strongly deviate from the uncoupled TC resonances and in the limit of zero thickness, they tend towards the uncoupled acoustic TC resonances with pressure release condition at the panel location.

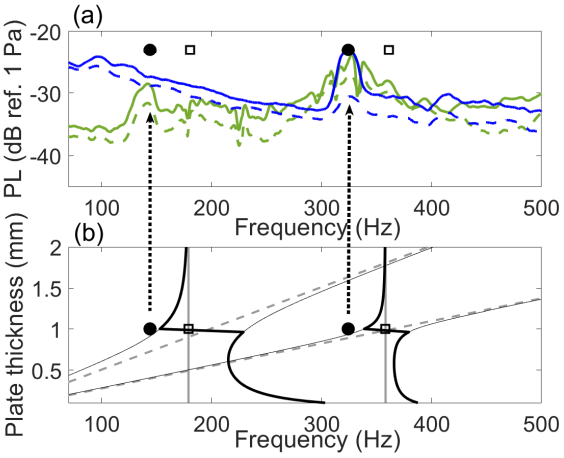

Figure 4. (a) Pressure levels (PL) measured over the (plain: solid; microperforated: dashed) floor of a cavity at 1.4 cm from its upstream edge under a low-speed TBL (blue) or under an acoustic excitation (green); (b) Plate thickness dependence of the resonance frequencies associated to the $(n_x,n_y)=(3,1)$ and $(5,1)$ clamped panel modes (dashed grey), to the $(n_x,n_y,n_z)=(0,0,1)$ and $(0,0,2)$ TC acoustic modes (solid grey) and to the fully-coupled TC–P modes given by Eq. (1) (solid black); the squares show the uncoupled TC resonance frequencies whereas the dots show the coupled TC–P resonances frequencies with $h_p = 1$ mm.

4. LATTICE-BOLTZMANN SIMULATIONS

A numerical model based on the 2D Lattice Boltzmann Method (LBM) [15,16,17] has been built to predict the effect on the TC resonances of microperforating the floor of a cavity in transitional flow regime. LBM simulations were performed on the flow cavity model shown in Fig. 5(a) in which a laminar boundary layer is incoming from

the inlet section with a free-stream velocity of $30.7\,\mathrm{m\,s^{-1}}$ towards the mouth of a transitional cavity with depth $D = 0.05\,\mathrm{m}$ and length $L = 0.53\,\mathrm{m}$. All the walls are rigid. The cavity floor is either plain or microperforated with sharp-edged apertures of width 0.5 mm so that the ratio of the aperture half-width to the viscous boundary layer thickness (Shear number) is the same as in the experiment. However, the apertures have a larger pitch, 62.5 mm instead of 5 mm, in order to keep the 2D perforation ratio as in the experiment, *e.g.* 0.8%. The tunnel height is $H = 0.24\,\mathrm{m}$. It is lower than in the experiment, $H = 0.9\,\mathrm{m}$, to save computational time. A free-slip boundary condition is imposed at the bottom wall located at $z = H + D = 0.245\,\mathrm{m}$ apart from the cavity floor. Open flow conditions are imposed at the outlet. At $z = -0.05\,\mathrm{m}$ behind the MPP no-flow side, there is a damping layer of artificially increased viscosity that emulates absorbing boundary conditions.

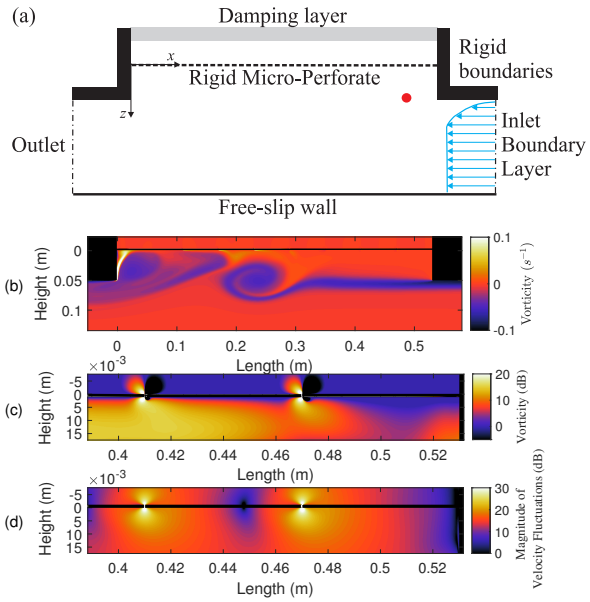

Figure 5. (a) The 2D geometry and boundary conditions for the Lattice Boltzmann Model of a transitional cavity undergoing a laminar boundary layer flow; the drawing only represents the central part of the computational domain that ranges from $x = -0.5\,\mathrm{m}$ to $x = 1.03\,\mathrm{m}$. (b) simulated snapshot of the vorticity over and within the cavity; (c) zoom of the vorticity across the microperforated floor right after the cavity upstream edge; (d) zoom of the velocity fluctuations over the same domain; clockwise (resp. counterclockwise) vortices are related to dark (resp. clear) colors in (c) and (d).

As seen in Fig. 5(b), the vortical flow structure is characterized by a roll-up of the shear layer that extends up to half of the cavity length from the leading edge. The shed vortices, with dimensions of nearly the cavity depth, reattach at a distance 31 cm from the leading edge. Fig. 5(c) show that outflow conditions occur across the first apertures from the MPP flow side towards the MPP no-flow side. These outflow conditions generate clockwise (resp. counterclockwise) vortex shedding at the inlet and outlet of the apertures right (resp. left) side. On the MPP flow side, the holes inlet vortices tend to merge with the near-wall vorticity whereas, on the MPP no-flow side, there are no convection effects and vortex shedding from the holes occurs parallel to the orifices axis. One observes in Fig. 5(d) that the maximum velocity fluctuations is localized within, but also at the inlet/outlet of the micro-perforations through vortex shedding. Thus, the latter mechanism appears to play a more important role in the attenuation than visco-thermal dissipation, given a Shear number comprised between 2.9 and 5.1 up to 1 kHz.

Figure 6 shows the effect of microperforating the floor of the transitional cavity on the simulated levels of the pressure fluctuations, here calculated at the red dot position shown in Fig. 5(a). For sake of convergence, the grid size required 80 cells per aperture width. This corresponds to a minimum number of 4 cells across the orifice viscous boundary layer at 3 kHz. The first dominant peak in Fig. 6 is predicted by the LBM at 703 Hz and occurs, as expected, between the first TC and tunnel (T) resonances, respectively at 694 Hz and 708 Hz. The second dominant peak at 1391 Hz is between the second TC and T resonances, respectively at 1388 Hz and 1416 Hz. These peaks occur at higher frequencies with respect to the dominant peaks observed in the experiment because the tunnel height, 0.24 m in the simulations, is lower than that in the wind-tunnel experiments.

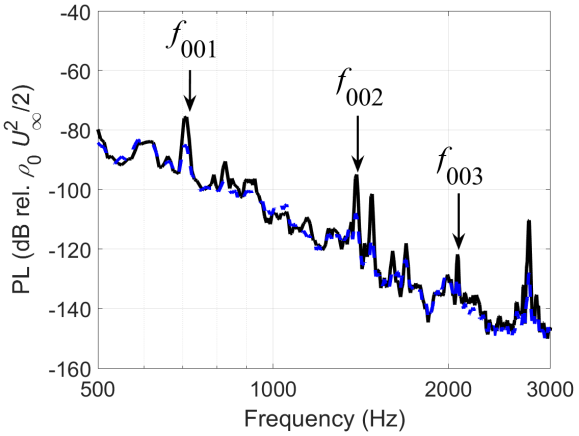

Figure 6. Pressure level (PL) spectra calculated by LBM at a horizontal distance 8.4 cm from the upstream edge at the mouth of a transitional flow cavity assuming a plain (solid black) or microperforated (dashed blue) floor.

It can be seen from Fig. 6 that the LBM model clearly captures the ability of the microperforations to attenuate the pressure fluctuations at the mouth of the cavity by up to 9 dB on the first dominant peaks. Although not shown, the predicted amount of attenuation at the cavity floor reaches up to 16 dB at the second peak: it obviously overestimates the measured attenuation that was not exceeding 8 dB on the second transverse mode at the cavity floor. Major hindering effects may be due to the 2D nature of the model that modifies the MPP apertures radiation conditions with respect to a 3D one as well as

extraneous sources of energy loss that are not modeled, but that are likely to occur such as acoustic propagation at the inlet and outlet of the test section or viscous dissipation at the wind-tunnel walls.

5. OPTIMISATION STUDY

Of interest is to optimise the constitutive parameters of the MPP base wall in order to maximize the attenuation of the pressure fluctuation levels. Direct MPP optimisation from the LBM simulations is cumbersome but impedance optimisation methods [18,19,20] appear well-suited. The MPP optimum impedance can be found to achieve maximum axial decay rate of the least attenuated duct mode. It has been derived by Cremer for a rectangular duct in the no-flow case [18] and generalised by Tester [19] for a circular duct in the "plug" flow case under the "well cut-on" modes assumption. This limitation has been overcome and exact expressions [20] have been derived of the optimum axial wavenumber and MPP optimal impedance in flow ducts in the low frequency range.

However, several factors may preclude the use of these methods in our problem. First, one needs a locally reacting base wall impedance. This is achieved below 323 Hz, *e.g.* when there is at most half-a-wavelength between the cavity side walls on the MPP no-flow side. Second, the flow needs to be uniform along the base wall. LBM simulations showed that this is not the case with peak values of the axial mean velocity nearby the MPP that stay lower (in magnitude) than $6\,\mathrm{m\,s^{-1}}$.

Despite these limitations, optimisation of the MPP impedance has been undertaken at 703 Hz, the first TC trapped mode, assuming a uniform flow of $6\,\mathrm{m\,s^{-1}}$ in a 2D rectangular waveguide of height 0.245 m between the MPP and the tunnel bottom wall. The optimum impedance was obtained from a graphical solution to the eigenvalue equation

$$-\mathrm{i}\,u_z \tan u_z \frac{\alpha^2 \mathrm{He}^2}{\left[\mathrm{He} + M\sqrt{\mathrm{He}^2 - \alpha^2 u_z^2}\right]^2} = \beta, \qquad (2)$$

where $\mathrm{He} = kH$ is the Helmholtz number, $\alpha = 1 - M^2$, $u_z = k_z H$, the transverse wavenumber in reduced form and $\beta = (kH) y_{\mathrm{MPP}}$ with $y_{\mathrm{MPP}} = z_{\mathrm{MPP}}^{-1} = Z_0 / Z_{\mathrm{MPP}}$ the MPP specific transfer admittance, Z_{MPP} the MPP transfer impedance and Z_0 the air characteristic impedance. Eqn. (2) was solved by plotting in the complex β-plane the locii of the axial attenuation, $\mathrm{Att} \approx 8.7\,\Re(u_z)$, when varying $\Re(u_z)$ between 0 and 2π and for several values of $\Im(u_z)$ comprised between 0.5 and 1, while u_z satisfies Eqn. (2) for a given β. For each value of $\Im(u_z)$, one observes in Fig. 7 looping curves. It can be seen in the complex β-plane that they intersect each other for an infinite number of eigensolutions u_z to Eqn. (2), each intersection corresponding to two modes with different attenuations for a given value of β, the first mode being the least attenuated. There is however a specific value of $\Im(u_z)$ at which the first loop collapses to a point, called the winding point, so that the two first modes merge at this point. They are therefore associated to the largest possible attenuation of the first mode.

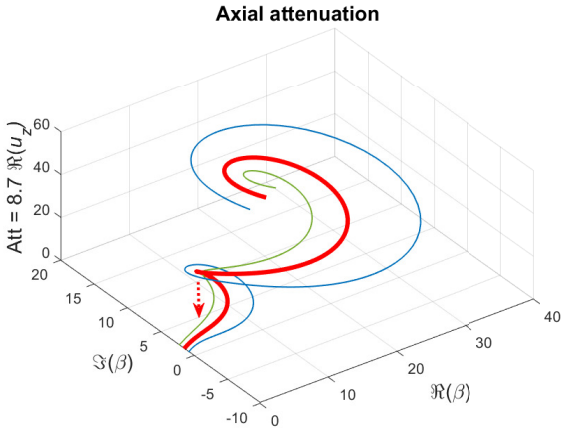

Figure 7. Variations of the axial attenuation as a function of the real and imaginary parts of β defined in Eqn. (2); each curve corresponds to a constant value of $\Im(u_z)$, respectively 0.50 (blue), 0.73 (red) and 0.94 (green), when $\Re(u_z)$ increases between 0 and 2π.

Once the optimal transverse wavenumber u_z^{opt} and the corresponding attenuation are graphically obtained, substitution into Eqn. (2) provides β_{opt} as well as the optimal MPP specific impedance $z_{\mathrm{MPP}}^{\mathrm{opt}} = \mathrm{He}\,\beta_{\mathrm{opt}}^{-1}$. The optimal axial wavenumber $k_{x,\mathrm{opt}}$ can be deduced from the following axial vs. transverse wavenumber relationship

$$\frac{k_x^{\mathrm{opt}}}{k} = -\frac{1}{\alpha}\left(M + \sqrt{1 - \alpha\left(\frac{u_z^{\mathrm{opt}}}{\mathrm{He}}\right)^2}\right), \qquad (3)$$

with the square-root evaluated in the complex upper-half plane. Note that, at low Mach number and for $\mathrm{He} << |u_z|$, the axial wavenumber in Eqn. (3) can be approximated by $k_x H \approx -\mathrm{i}\,u_z$, so that the axial attenuation per unit length, $\mathrm{Att} = -8.7\,\mathrm{Im}(k_x H)$, is close to $\mathrm{Att} \approx 8.7\,\mathrm{Re}(u_z)$.

The MPP optimisation process required 3 steps:

- In a first step, the above graphical optimization method is performed and provides at 703 Hz, under a Mach number $M = 0.018$, a MPP optimal specific transfer impedance given by

$z_{\mathrm{MPP}}^{\mathrm{opt}} = (0.943 - \mathrm{i}\,0.737)\,\mathrm{He}/\pi$, that slightly overestimates the theoretical Cremer optimal impedance $z_{\mathrm{MPP}}^{\mathrm{opt}} = (0.929 - \mathrm{i}\,0.744)\,\mathrm{He}/\pi$ [18], as already observed in [20].

- In a second step, exhaustive search has been carried out to find the MPP constitutive parameters, respectively the thickness t_h, the holes diameter d_h and the perforation ratio σ that lead to a MPP specific resistance, $r = \Re(z_{\mathrm{MPP}})$, as close as possible to its optimal value $\Re(z_{\mathrm{MPP}}^{\mathrm{opt}})$. The following model was used for the MPP specific resistance [21]

$$r = \Re(z_{\mathrm{MPP}}^{\mathrm{in}}) + \frac{8}{\sigma c_0}\sqrt{\frac{\omega\nu}{2}} + \frac{K|M|}{\sigma}, \qquad (4)$$

with

$$z_{\mathrm{MPP}}^{\mathrm{in}} = \frac{\mathrm{i}\omega t_h}{\sigma c_0}\left(1 - \frac{2}{k_h\sqrt{-\mathrm{i}}}\frac{J_1(k_h\sqrt{-\mathrm{i}})}{J_0(k_h\sqrt{-\mathrm{i}})}\right)^{-1}, \qquad (5)$$

where $z_{\mathrm{MPP}}^{\mathrm{in}}$ is the inner overall specific MPP impedance, the second term representing added external resistance for sharp edged holes and the last term added resistance induced by the grazing flow over the MPP with $K = 0.15$ [21]. In Eqn. (5), ν is the kinematic viscosity and k_h is the Shear number. Here, the optimal resistance was achieved for the following parameters, $t_h = 1\,\mathrm{mm}$, $d_h = 0.7\,\mathrm{mm}$ and $\sigma = 1.18\,\%$, corresponding to a holes pitch $u_h = 5.7\,\mathrm{mm}$.

- In a third step, a LBM simulation was run with these optimized MPP parameters.

The results are shown in Fig. 8 for the attenuation spectra and in Fig. 9 for the spatial distribution of the pressure levels over the cavity floor considering nominal and optimized MPPs. The attenuation was calculated at a distance from the upstream edge such that the axial mean flow velocity peaked at $6\,\mathrm{m\,s^{-1}}$ which corresponds to the assumed flow speed. Figure 8 shows that the optimized MPP enhances at 703 Hz the attenuation by 13 dB with respect to the nominal MPP. Above 800 Hz, the optimized MPP does not outperform the nominal MPP and even appears to generate extra noise above 1 kHz. Below 703 Hz, the attenuation bandwidth is extended in the region of the plane wave least attenuated mode, especially below 321 Hz where the MPP is locally-reacting. The dashed blue curve in Fig. 9 shows the pressure spatial distribution of the (2,0) streamwise mode that emerges once the tunnel mode at 703 Hz has been significantly damped by the nominal MPP. Optimizing the MPP further reduces the amplitude of this mode by 14 dB, but only in a local zone where the axial mean flow velocity reaches $6\,\mathrm{m\,s^{-1}}$.

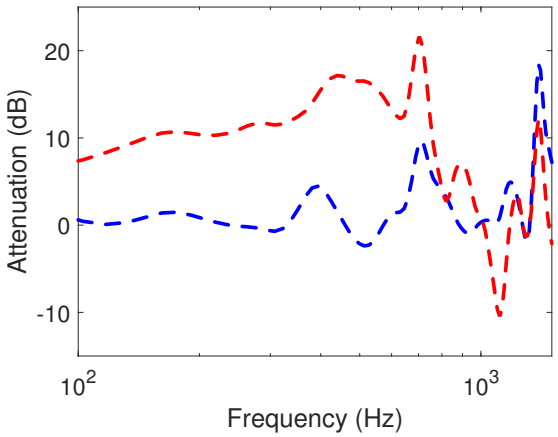

Figure 8. Attenuation of the pressure levels by a nominal (dashed blue) and optimized (dashed red) MPP floor when calculated on the base wall at 0.2 m apart from the cavity upstream edge.

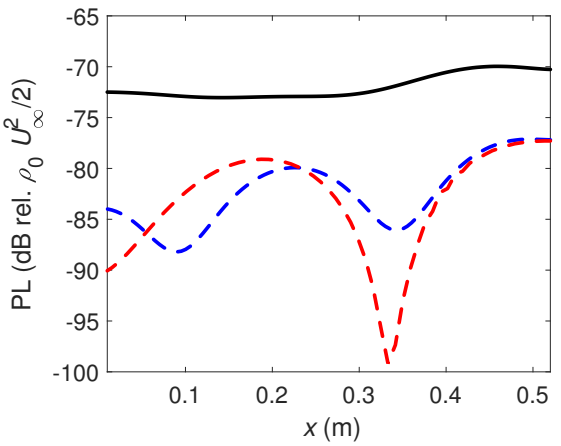

Figure 9. Spatial variation of the pressure levels (PL) along the cavity base wall at 703 Hz, frequency at which the MPP has been optimized: plain (solid black), nominal (dashed blue) and optimized (dashed red) MPP floors.

6. CONCLUSIONS

Experimental and numerical studies have been performed to evaluate the effect on the pressure fluctuations of microperforating the floor of shallow cavities at low Mach number in transitional flow regime. Wind-tunnel measurements showed that the amplitude of the first dominant pressure peaks that occur towards the leading edge of the cavity floor were attenuated by the MPP. This was qualitatively supported by aeroacoustic simulations based on a 2D LBM that predicts the pressure and velocity fluctuations within the cavity and across the MPP. More specifically,

- Measurements of wall-pressure spectra performed at Mach 0.09 at the bottom of a transitional flow cavity showed dominant peaks on one third of the cavity floor towards the leading edge. The peaks are linked to cut-on transverse Tunnel-Cavity resonances excited by the shear layer, trapped within the cavity test section and coupled with the base wall flexural modes. Elasto-acoustic coupling with the thin panel flexural modes induced a significant downshift of the first TC resonance frequencies.

- Microperforating the floor of the transitional cavity in the wind-tunnel experiments led to maximum 8 dB attenuation on the first peak levels. The MPP effect has been simulated by a 2D LBM model assuming a low-speed laminar boundary layer for a cavity in a transitional flow regime and without elasto-acoustic coupling. Assuming a number of 80 cells per aperture width (0.5 mm), the LBM well predicts an attenuation of the dominant peaks at the cavity floor and mouth, but overestimates the amount of attenuation with respect to that observed in the experiment. It shows that vortex shedding at the inlet-outlet of the base wall apertures plays an important role in the dissipation mechanism.

- Optimisation of the MPP cavity floor has been performed such that the input impedance achieves maximum axial decay rate of the least attenuated TC mode at its resonance frequency. This mode was already attenuated by the MPP, but the optimized treatment locally brought further reduction and extended the bandwidth of attenuation well below the first TC cut-on frequency.

3D LBM simulations should be implemented to better correlate the MPP attenuation levels with respect to the wind-tunnel measurements. The optimisation study could also account for the shape of the MPP holes, for instance considering slanted or tapered holes geometries in order to increase the dissipation of energy at the TC resonances.

7. ACKNOWLEDGMENTS

This study was funded in Spain by the Ministerio de Economía y Competitividad project TRA2017-87978-R, AEI/FEDER, UE, and the mobility program ILINK+2018. It was supported in France by the ANR VIRTECH (ANR-17-CE10-0012) and by the Labex MEC, Excellence Initiative of Aix-Marseille University - A*MIDEX, a French "Investissements d'Avenir" programme.

8. REFERENCES

[1] K. D. Sakaliyski, J. I. Hileman and Z. S. Spakovsky: "Aero-acoustics of perforated drag plates for quiet transport aircraft," *Proceedings of the 45th AIAA Aerospace Science Meeting and Exhibit*, AIAA 2007-1032, 2007.

[2] K. Tanner, N. Mackenzie, R. Jones and Y.-K. Lee: "Aeroacoustic assessment of facades," *Proceedings of Acoustics 2016, the 2nd Australasian Acoustical Societies Conference*, Paper 149, 2016.

[3] X. Yu, L. Cheng and J.-L. Guyader: "Modeling vibroacoustic systems involving cascade open cavities and micro-perforated panels," *Journal of the Acoustical Society of America*, Vol. 136, pp. 659–670, 2014.

[4] C. Lada and K. Kontis: "Experimental Studies on Transitional and Closed Cavity Configurations Including Flow Control," *Journal of Aircraft*, Vol. 47, pp. 723–730, 2010.

[5] X. Gloerfelt, Cavity noise, uploaded the 11/03/2020 from: https://www.researchgate.net/publication/265080835_CAVITY _NOISE.

[6] X. Amandolèse, P. Hémon and C. Regardin: "A study of the acoustic oscillations by flow over cavities," *ASME Journal of Vibration and Acoustics*, Vol. 126, pp. 190–195, 2004.

[7] P. Lafon, S. Caillaud, J. P. Devos and C. Lambert: "Aeroacoustical coupling in a ducted shallow cavity and fluid/structure effects on a steam line," *Journal of Fluids and Structures*, Vol. 18, pp. 695–713, 2003.

[8] T. Emmert, P. Lafon and C. Bailly: "Numerical study of aeroacoustic coupling in a subsonic confined cavity," *Proceedings of the 14th AIAA/CEAS Aeroacoustics Conference*, AIAA 2008-2848, 2008.

[9] C. Maury, T. Bravo, and D. Mazzoni: "The use of microperforations to attenuate the cavity pressure fluctuations induced by a low-speed flow," *Journal of Sound and Vibration*, Vol. 439, pp. 1–16, 2019.

[10] J. O. Alvarez and E. J. Kerschen: "Influence of Wind Tunnel Walls on Cavity Acoustic Resonances," *Proceedings of the 11th AIAA/CEAS Aeroacoustics Conference*, AIAA 2005-2804, 2005

[11] K. Aly and S. Ziada: "Flow-excited resonance of trapped modes of ducted shallow cavities," *Journal of Fluids and Structures*, Vol. 26, pp. 92–120, 2010.

[12] T. Bravo, C. Maury, and C. Pinhède: "Absorption and transmission of boundary layer noise through flexible multi-layer micro-perforated structures,"

Journal of Sound and Vibration, Vol. 395, pp. 201–223, 2017.

[13] J. Pan and D. A. Bies: "The effect of fluid-structural coupling on sound waves in an enclosure – theoretical part," *Journal of the Acoustical Society of America*, Vol. 87, pp. 691–707, 1990.

[14] F. Fahy and P. Gardonio: "Acoustic Coupling between Structures and Enclosed Volumes of Fluid," *Sound and Structural Vibration*, Academic Press, 2nd Edition, 2007.

[15] G. R. McNamara and G. Zanetti: "Use of the Boltzmann equation to simulate lattice-gas automata," *Physical Review Letters*, Vol. 61, pp. 2332–2335, 1988.

[16] P. L. Bhatnagar, E. P. Gross and M. A. Krook: "A model for collision processes in gases. I. Small amplitude processes in charged and neutral one-component systems," *Physical Review*, Vol. 94, pp. 511–525, 1954.

[17] A. T. de Jong, H. Bijl, A. Hazir and J. Wiedemann: "Aeroacoustic simulation of slender partially covered cavities using a Lattice Boltzmann method," *Journal of Sound and Vibration*, Vol. 332, pp. 1687–1703, 2013.

[18] L. Cremer: "Theory regarding the attenuation of sound transmitted by air in a rectangular duct with an absorbing wall, and the maximum attenuation constant produced during this process," *Acta Acustica united with Acustica,* Vol. 3, pp. 249–263 (In German), 1953.

[19] B. J. Tester: "The propagation and attenuation of sound in lined ducts containing uniform or "plug" flow," *Journal of Sound and Vibration*, Vol. 28, pp. 151–203, 1973.

[20] R. Kabral, L. Du and M. Åbom: "Optimum sound attenuation in flow ducts based on the "exact" Cremer impedance," *Acta Acustica united with Acustica*, Vol. 102, pp. 851–860, 2016.

[21] S. Allam and M. Åbom: "A new type of muffler based on microperforated tubes," *ASME Journal of Vibration and Acoustics*, Vol. 133, 031005-1:8, 2011.